# Effect of transport limitations and fluid properties on reaction products in fractures of unaltered and serpentinized basalt exposed to high $P_{CO_2}$ fluids

CrossMark

Jubilee T. Adeoye[a], Anne H. Menefee[a], Wei Xiong[b], Rachel K. Wells[c], Philip Skemer[c], Daniel E. Giammar[b], Brian R. Ellis[a,*]

[a] Department of Civil and Environmental Engineering, University of Michigan, United States
[b] Department of Energy, Environmental and Chemical Engineering, Washington University in St. Louis, United States
[c] Department of Earth and Planetary Sciences, Washington University in St. Louis, United States

A B S T R A C T

A series of high temperature and high pressure (45 °C and 100 °C; 10 MPa) experiments were conducted to examine geochemical alterations of fractured serpentinized and unaltered basalts exposed to high $_{P_{CO_2}}$ fluids. Net mineral dissolution was observed in flow-through experiments that examined reactions under advection-dominated conditions, whereas carbonate mineral precipitation occurred along basalt fractures after 6 weeks of reaction in static batch experiments where mass transport was diffusion limited. Consistent with prior work, increased temperature and salinity enhanced dissolution in flow-through experiments, and greater congruency in silicate dissolution was observed at higher temperature. Analysis of the reacted cores via X-ray computed tomography revealed regions of enhanced dissolution along the fracture pathway that correspond to contact with large grains of pyroxene and olivine. In the batch experiments, discrete Mg-bearing siderite crystals were observed along the entire fracture of the fine-grained unserpentinized basalt samples, while siderite formed in clusters along the fracture of the coarser-grained serpentinized basalt. Results of this study demonstrate how diffusive mass transport conditions and distribution of reactive mineral phases may be key factors in determining the extent of silicate dissolution and secondary mineral carbonation during geological carbon sequestration in fractured basalts.

## 1. Introduction

Geological carbon sequestration has been identified as a strategy to mitigate anthropogenic $CO_2$ emissions in an effort to curtail global climate change (Intergovernmental Panel on Climate Change, 2005). Until recently, most research efforts have focused on storage in sedimentary formations such as depleted oil and gas reservoirs (e.g., Shaw and Bachu, 2002; Jenkins et al., 2011; Whittaker et al., 2011) and deep saline aquifers (e.g., Bachu and Adams, 2003; Nordbotten et al., 2005; Michael et al., 2010; Szulczewski et al., 2012). While these reservoirs are ubiquitous and offer large storage capacities, a majority of the stored $CO_2$ will be trapped via structural or residual trapping mechanisms, with minimal mineral trapping due to limited abundance of reactive metal ions (Johnson et al., 2004; Benson and Cole, 2008) and slow dissolution kinetics of siliciclastic minerals (Xu et al., 2005; Wigand et al., 2008). In contrast, substantial mineral trapping of injected $CO_2$ can occur in basaltic formations, which commonly include minerals such as olivine and pyroxene that are highly reactive with

$CO_2$-rich fluids (Knauss et al., 1992; Wang and Giammar, 2013). Dissolution of these minerals is promoted under low pH conditions and will release divalent metal cations to solution (e.g., $Ca^{2+}$, $Mg^{2+}$, $Fe^{2+}$), which can combine with dissolved inorganic carbon to form stable carbonate minerals. Recent studies have demonstrated rapid mineral carbonation in basalt following the injection of $CO_2$ pre-dissolved in water at the CarbFix site in Iceland (Matter et al., 2016) and pressurized liquid $CO_2$ at the Wallula Basalt Pilot Project in Washington state (McGrail et al., 2017). In both cases, secondary carbonate precipitates were observed within two years and chemically correlated with the injected $CO_2$ (Matter et al., 2016; McGrail et al., 2017). The success of these field validations motivates continued investigations into fundamental processes governing $CO_2$-water-basalt interactions.

The dissolution of host minerals in the basalt reservoir and subsequent precipitation of carbonate minerals will result in a net increase in the bulk volume of the rock relative to its initial volume (Kelemen et al., 2011; Xiong and Giammar, 2014). Such mineral precipitation may clog or completely close flow pathways and inhibit continued $CO_2$

injection (Hövelmann et al., 2012; Sokama-Neuyam and Ursin, 2015). However, this mineral carbonation may also lead to reaction-induced fracturing within the reservoir, a process described as 'reactive cracking' (Kelemen et al., 2013; Zhu et al., 2016). Mineral precipitation-induced fracturing might enhance the $CO_2$ sequestration potential of basalt reservoirs and the long-term injectivity of $CO_2$ in basalt formations by generating new reactive surfaces for further mineral dissolution, effectively increasing reservoir storage capacity (Kelemen et al., 2011; Hövelmann et al., 2012).

Batch experiments on rocks from the Colombia River Basalt Group show that mineral reactivity is dependent on *in situ* fluid properties such as temperature, $CO_2$ pressure ($P_{CO2}$), pH, and salinity (Schaef and McGrail, 2009; Schaef et al., 2010). Sissmann et al. (2014) found that olivine ($(Mg,Fe)_2SiO_4$) and pyroxene ($(Mg,Ca,Fe)_2Si_2O_6$) dissolve preferentially under acidic conditions, favoring the release of Mg and Fe into solution, while plagioclase ($CaAlSi_3O_8$) dissolution is favored above circumneutral pH. It has also been shown that the effect of $P_{CO2}$ on the dissolution of olivine is only significant to the extent that it impacts the pH of the solution, as $P_{CO2}$ alone will not enhance dissolution of silicate minerals under fixed pH conditions (Brady and Carrol, 1994; Giammar et al., 2005; Prigiobbe et al., 2009). Although Prigiobbe et al. (2009) concluded that salt concentration does not have an independent effect on the dissolution of olivine grains, Wang and Giammar (2013) found that forsterite dissolution was enhanced by NaCl due to the potential inhibition of silica-rich surface layers that have been shown to impede dissolution. This is significant because dissolution of silicate minerals has been identified as the rate limiting step for mineral carbonation under $CO_2$ sequestration conditions (Giammar et al., 2005; Matter et al., 2007; Prigiobbe et al., 2009; Van Pham et al., 2012). Several studies have reported enhanced silicate dissolution with an increase in temperature in accordance with the Arrhenius equation (Galwey and Brown, 2002; Laidler, 1984). H & velmann et al. (2012) reported enhanced precipitation and more developed carbonate crystal formation with increasing temperature (from 100° C to 200 °C) and time of reaction in peridotite cubes under static batch conditions. Rosenbauer et al. (2012) carried out a combined batch experiment and modeling study on two tholeiitic basalts over a temperature range of 50–300 °C at 300 bar $P_{CO2}$ and found that the extent and rate of reaction were greatest at 100 °C. Gysi and Stefánsson (2012) carried out batch experiments and modeling studies on natural basaltic glass at 75, 150, and 250 °C, and found that mineral carbonation was most favorable at 75 °C. This favorability of mineral carbonation at temperatures below 100 °C was associated with the tendency for Mg and Fe to be incorporated into clays at temperatures greater than 100 °C, limiting the availability of the metal ions for carbonate mineralization.

The extent of mineral dissolution and secondary carbonate precipitation during $CO_2$ sequestration in basaltic reservoirs will also be impacted by mass transport conditions within the fractured rock (Xiong and Giammar, 2014). Yang et al. (2013) reported magnesite precipitation in regions of a forsterite-packed capillary tube where mass transfer was controlled by diffusion; precipitation was not observed in the main channels with advection-dominated transport. Giammar et al. (2014) showed that while the volume-averaged properties of a packed bed of forsterite remained undersaturated with respect to magnesite in the presence of $CO_2$-rich water, locally supersaturated conditions developed in diffusion-limited zones. Similar to Xiong and Giammar (2014) who found that carbonation was spatially localized in the diffusion limited zone of a packed forsterite bed, Andreani et al. (2009) concluded that precipitation is favored in fractures with limited or reduced mass flow such as dead-end zones where diffusion dominates over advection. Conversely, dissolution dominates in zones of higher flow rate, which induces the development of silica-rich passivating layers that inhibit dissolution and thus limit the potential for mineral carbonation. Under advective transport conditions in olivine-rich basalt, Peuble et al. (2015) found the carbonation rate per unit mass of rock was enhanced at higher flow rates, although more $CO_2$ was carbonated per unit fluid volume at lower flow rates. While these studies identify the importance of transport processes for mineral precipitation in mafic rocks, there remains a need to study the role of mass transport limitations coupled with mineral distribution in controlling $CO_2$ carbonation in fractured basalts. Separating diffusive and advective transport regimes is crucial to understanding how mass transport conditions affect dissolution and precipitation of minerals under sequestration conditions in fractured basalts.

The objective of this study was to investigate the role of fluid transport regimes on the dissolution of mafic minerals and precipitation of secondary carbonates in fractures of serpentinized and unaltered basalt cores. A series of flow-through and batch experiments were designed to decouple advection- and diffusion-dominated transport under similar *in situ* fluid and temperature conditions. Differences in transport regime along with variances in basalt composition and mineral grains size were correlated with observed reaction products to investigate critical factors promoting $CO_2$ mineralization in basalts.

## 2. Materials and methods

### 2.1. Basalt sample characterization

Two different basalts, an unaltered basalt from the Columbia River flood basalt near Pullman, Washington, and a serpentinized basalt from a basalt dike near Valmont Butte, Colorado (hereafter referred to as UB and SB, respectively), were examined in this study. Serpentinization is a process through which ultramafic rocks are altered by the inclusion of water into the crystal structures of the divalent cation-bearing minerals in the rock (Berndt et al., 1996; Frost and Beard, 2007).

Standard ($\sim 30\,\mu m$ thick) petrographic thin sections were made of each sample. Optical and electron microscopy, including the electron microprobe (JEOL JXA-8200), were used to examine the texture and mineralogy of the sample. Grain size and mineral percent abundances were estimated through analysis of energy dispersive spectroscopy (EDS) and backscatter electron microscopy (BSE) images via ImageSXM. Compositional analysis of individual minerals was completed via wavelength dispersive spectroscopy (WDS).

### 2.2. Sample preparation

Several 2.54 cm diameter cores were generated from 42 to 45 mm thick slabs of the bulk sample material through the use of a diamond core drill. Each core was cut into two half-cylinder sections using a precision saw with a diamond blade. For the flow-through experiments, the surface of one half-cylinder was polished flat with 400 grit sandpaper, while the other half-cylinder was etched with a ~1 mm-wide meandering pattern (Fig. 1a) using a CNC milling machine (Roland Model MDX-40a) with a 0.5 mm diamond bur. The etched surface was polished with 400 grit sandpaper until the pattern depth reached the target of 95–105 $\mu m$. The pattern depth was determined by comparing the z-value of the spots on the groove and the spots on the closest polished surface in an optical microscope (ZEISS, Observer.Z1). The meandering etched pattern served as a flow path for the injected fluid and was designed to increase the fluid residence time. This design increased the flow path to ~6 times the length of the cylindrical core. Assembled core halves for the flow-through experiments were coated with epoxy on the sides parallel to the direction of flow and encased in chemical-resistant heat shrink tubing. For the static batch experiments, a straight groove design with a width of 11 mm and target depth of 95–105 $\mu m$ (Fig. 1b) was etched on the saw-cut surface of the core to provide an increased reaction volume. Assembled core halves prepared for static batch studies were coated with epoxy (MasterBond EP42HT-2) on all sides except the top surface to ensure unidirectional diffusion of fluid into the fracture, thus mimicking a dead-end fracture.
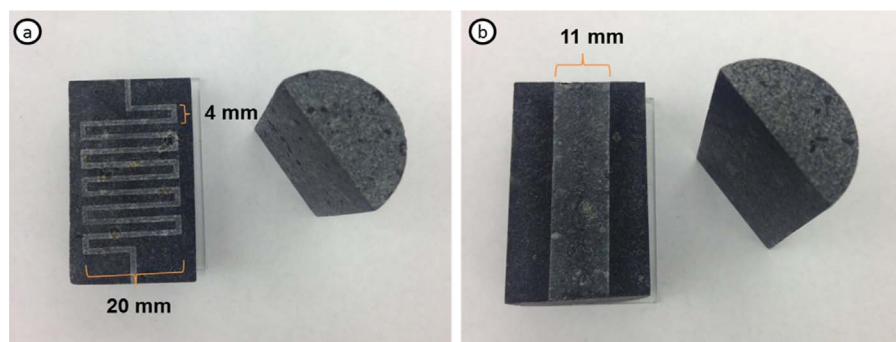
**Fig. 1.** Engineered fracture patterns including (a) meandering groove used in the flow-through study, and (b) straight groove used in the static batch experiments. Fracture dimensions are also labelled. Both fracture configurations are approximately 100 μm deep.

### 2.3. Flow-through experiment setup

The flow-through apparatus includes a core flooding cell and a batch reactor for equilibrating influent solutions with high-pressure $CO_2$ prior to injection. Water was saturated with $CO_2$ within a 600-mL stainless steel batch reactor (Parr Instrument) under a constant $CO_2$ pressure of 10 MPa for at least 24 h prior to initiating flow through the fractured basalt samples. The batch reactor was heated externally by a heating jacket attached to a controller to maintain *in situ* temperature within ± 1 °C of the set temperature. The two half-cylinder sections of the basalt cores were secured in chemical–resistant heat shrink tubing and placed in a viton sleeve before being subjected to a confining stress of 20 MPa in a biaxial core flooding cell (Core Laboratories). $CO_2$-acidified water was injected at a constant rate of 5 mL/h, corresponding to a residence time of approximately 16 s in the etched channel, and discrete effluent samples aggregated over 1–2 h were collected for a duration of 120 h. Differential pressure was monitored throughout the experiment by pressure transducers installed upstream and downstream of the flow cell. A back pressure regulator was used to prevent *in situ* degassing of $CO_2$ and to maintain a constant system back pressure of 10 MPa.

Table 1 lists the three experimental conditions tested for each basalt type. The first two experiments were carried out with deionized (DI) water with resistivity greater than 18.2 MΩ-cm, but temperature was raised from 45 °C to 100 °C in the second. In actual systems, temperature depends on the geothermal gradient and storage depth; sites are typically selected to exceed the critical point for $CO_2$ (31.6 °C and 7.3 MPa) (Bachu, 2000; McGrail et al., 2006; Schaef and McGrail, 2009). Higher temperatures were applied in the experiments to enhance reactivity over shorter time scales. The third flow-through experiment was also run at 100 °C and used a solution with salinity and alkalinity representative of a typical basalt reservoir in the U.S. Pacific Northwest based on hydrochemical data for Pasco Basin basalt aquifers collected at depths relevant to $CO_2$ storage (greater than 800 m) with reported charge balances within 10% error (Reidel et al., 2002). Because Na and Cl were the dominant cations and anions in these samples, the average Na concentration was selected along with the average alkalinity (as $HCO_3^-$) to create a simplified representative brine for this study. These levels of salinity and alkalinity were matched by adding 1.2 mM of $NaHCO_3$ and 13.8 mM of NaCl to DI water prior to brine equilibration in the batch reactor.

**Table 1**
Flow-through experiment conditions for serpentinized and unserpentinized basalt.

| Experiment | Water Composition | Temperature (°C) | $CO_2$ pressure (MPa) |
|---|---|---|---|
| SB/UB-1 | DI water | 45 | 10 |
| SB/UB-2 | DI water | 100 | 10 |
| SB/UB-3 | 1.2 mM $NaHCO_3$ 13.8 mM NaCl | 100 | 10 |

### 2.4. Static batch experiment design

Five epoxy-coated saw-cut cores of each basalt type were stacked on a multilevel sample rack, which was placed inside a 600-mL stainless steel pressure vessel (Parr Instrument) with a PTFE liner. 320 mL (64 mL per core) of DI water was added at the beginning of the reaction to maintain a rock to water ratio of 1:3 by volume in the reactor. The ratio of water volume to surface area within the fracture was ~1:200 $(cm^3/cm^2)$. $P_{CO_2}$ in the vessel was raised to 1 MPa and degassed 3 times to flush out residual $O_2$ in the headspace. The temperature in the vessels was then elevated to 100 °C using a heating jacket, while a syringe pump (500D, Teledyne Isco) was used to maintain $CO_2$ pressure at 10 MPa in the headspace. The initial volume of $CO_2$ in the headspace was approximately 85 mL. Batch results presented in this study are for cores and aqueous samples retrieved from the vessel after 6 weeks of reaction.

### 2.5. Analysis of effluent samples

Aliquots of the effluent from the flow-through experiments and post-experiment grab samples from the batch reactor were filtered through a 0.22 μm PVDF filter and acidified with $HNO_3$ to a pH < 2 prior to cation analysis (Ca, Mg, Fe, Si, Na, K, and Al) via inductively coupled plasma-mass spectrometry (7500ce & 7900 Agilent Technologies, CA). $CO_2$ solubility under each set of experimental conditions was calculated per the thermodynamic model presented by Duan and Sun (2003). Equilibrium constants were adjusted to system temperature and pressure conditions using SUPCRT92 with the DPRONS92 database (Johnson et al., 1992). Solution pH was calculated at each sampling point based on measured concentration of cations and anions with the constraint of electro-neutrality. Activity corrections for the experiments with added salinity and alkalinity were estimated by use of the Davies equation at 100 °C.

### 2.6. Characterization of reaction products

An optical microscope (LEICA, DFC295) was used to detect precipitates along the surface of the straight-etch groove in the samples from the batch system after six weeks of reaction. The precipitates were then scanned using Raman spectroscopy (HoloLab Series 5000 Laser Raman Microprobe, Kaiser Optical) with a 532 nm laser and a 20 power objective that probes a 5 μm diameter area. Raman spectra of carbonate mineral standards were obtained from the RRUFF database (Siderite R050349, Calcite R040070, Magnesite R040114). Scanning electron microscopy and energy dispersive X-ray spectroscopy (SEM-EDS, FEI Nova 230) were used to examine the precipitate morphology and elemental composition. The abundance of carbonate on the fracture surface was assessed via a point counting station (LEICA, DM2700p) for semi-quantitative analysis of precipitate distribution. The number of observable precipitates was counted in 100-μm wide steps across the fracture surface at depths ranging between 1 and 35 mm below the open end of the fracture.

## 2.7. X-ray computed tomography

Post-reaction X-ray computed tomography scans (XTH225, Nikon Metrology, Inc.) of the cores from the flow-through experiment were taken to infer dissolution patterns along the fracture pathway. These scans used a beam energy of 190 KV and current of 134 μA. 3141 projections were taken at steps of 0.11° with a 4-frame integration per projection. The data were reconstructed using CT Pro (XT5.1.3, Nikon Metrology, Inc), and ImageJ (National Institutes of Health, Bethesda, Maryland) was used to characterize changes in fracture geometry along the flow path.

## 3. Results

### 3.1. Initial mineralogical characterization

The UB sample is fine-grained with an average grain diameter of 50–100 μm, contains few vesicles, and is structurally homogeneous. The basalt consists of olivine ($Mg_{1.21}Fe_{0.78}Ca_{0.01}SiO_4$); pyroxene ($Ca_{0.63}Fe_{0.48}Mg_{0.83}Ti_{0.03}Al_{0.09}Si_{1.92}O_6$); plagioclase feldspar ($Ca_{0.59}$-$Na_{0.40}Fe_{0.03}Al_{1.57}Si_{2.40}O_8$); and a Si- and K-rich matrix comprised of grains that are too fine to be clearly observed under the electron microprobe. The Ca-rich nature of the pyroxene classifies it as diopside, while the Ca-Na ratio of the feldspar indicates labradorite. Illmenite ($FeTiO_3$) is also observed as an accessory mineral while orthopyroxene (($Mg,Fe)_2Si_2O_6$) is rare. The most common mineral assemblages in this sample are labradorite (31%) and the K-rich matrix (33%), while the olivine and diopside comprise 9% and 22% of the material, respectively. Approximately 1% of the olivine was serpentinized, suggesting this material is relatively unaltered. The least abundant minerals are ilmenite (3%) and orthopyroxene (1%).

The SB sample is somewhat coarser-grained compared to the UB, with an average grain diameter of 100–150 μm and occasional large phenocrysts. The mineralogy is composed of olivine ($Mg_{1.38}Fe_{0.59}Mn_{0.02}Si_{1.01}O_4$); pyroxene ($Ca_{0.83}Fe_{0.25}Mg_{0.85}Ti_{0.03}Al_{0.07}Si_{1.96}O_6$); plagioclase feldspar ($Ca_{0.55}Na_{0.43}Fe_{0.02}Al_{1.57}Si_{2.43}O_8$); and a Si- and K-rich matrix. Accessory minerals found in the serpentinized basalt include apatite ($Ca_5(PO_4)_3(Cl,OH)$), chromite ($FeCr_2O_4$), and glass ($SiO_2$). Similar to the unserpentinized basalt, the most common minerals in the SB are the labradorite and the matrix at 28% and 32%, respectively, followed by the Ca-rich pyroxene (diopside) at 21% and serpentine at 14%. While the majority of the olivine is serpentinized, 1% of the rock remains as unserpentinized olivine. As previously noted, serpentinized olivine is expected to be far less reactive than the unaltered olivine abundant in the flood basalt samples. Orthopyroxene comprises 1% of the SB, while accessory minerals only fill 3%. EDS maps for both basalts along with a comparison of mineral distributions are provided in Fig. 2 (Wells et al., 2016).
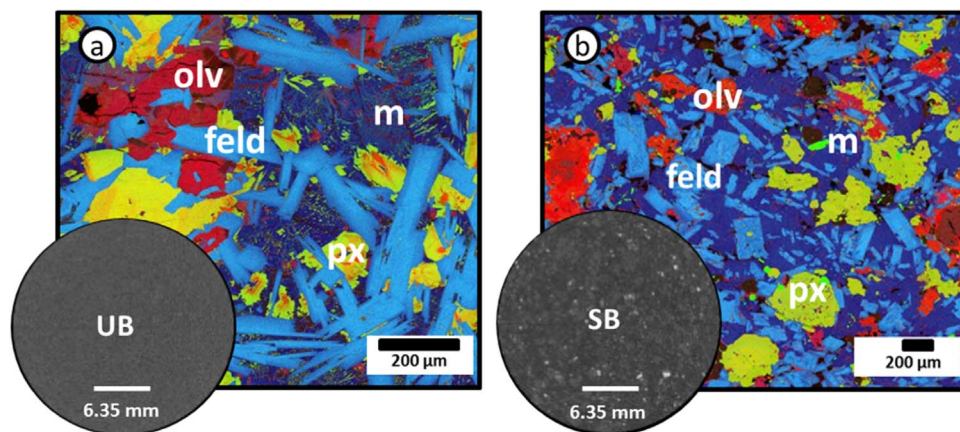
### 3.2. Flow-through study

#### 3.2.1. Evolution of effluent chemistry and pH

Figs. 3 and 4 present effluent cation concentrations over time for the SB and UB flow-through experiments, respectively. In the SB runs, calcium and magnesium displayed similar early spikes in concentration that peaked around 6 h followed by a decline toward quasi-steady-state conditions. Similar trends were observed for the UB with Ca and Mg peaking after 2–3 h. In all six experiments, Fe increased most rapidly over the first 3–6 h but leveled off after 20 h. Concentrations of the remaining cations analyzed were consistently lower than Ca, Mg, and Fe. Na and K leaching exhibited similar trends to those of Ca and Mg, while Al concentrations were about an order of magnitude lower than Ca and Mg with inconsistent trends across different experimental conditions. Consistent with prior work and the kinetics of silicate mineral dissolution, higher effluent concentrations were generally observed at higher temperatures (Giammar et al., 2005; Hänchen et al., 2006), and effluent concentration was enhanced with increases in salinity and alkalinity. Iron was the only cation that failed to follow these trends, as concentrations were highest at 45 °C in the SB and comparable between UB-1 (45 °C) and UB-3 (100 °C). For all cations, changes in temperature had little effect on the time required to reach quasi-steady-state conditions. Dissolved Ca and Mg concentrations were increased to a greater degree with the addition of salinity and alkalinity in the influent fluid than with an increase in temperature from 45 to 100 °C (Figs. 3 and 4).

The evolution of pH was similar for all three flow-through experiments (Figs. 3 and 4). Near steady-state conditions were achieved faster for UB (around 20 h) than for SB (40–60 h) samples. Initial pH was slightly higher in the SB cores, corresponding to a greater amount of initial mineral dissolution, but final pH values were comparable for both samples. The pH increased at 100 °C due to reduced $CO_2$ solubility at higher temperatures and was also elevated in experiments with added $NaHCO_3$.

Analysis of effluent solution chemistry and estimated in situ pH conditions indicate that all carbonate minerals were below saturation throughout all flow-through experiments (Fig. 5). Although more Ca and Mg dissolved than Fe, the systems were closest to saturation with respect to siderite as opposed to calcite or magnesite. Under the low pH conditions of the experiments, the solubility product of siderite is roughly two orders of magnitude smaller than that of the other carbonate minerals. Thus, siderite saturation will be achieved first given the similar concentrations of major divalent cations ($Fe^{2+}$, $Ca^{2+}$, $Mg^{2+}$).

#### 3.2.2. Extent of mineral dissolution

Mass balance calculations based on effluent chemistry were used to estimate net changes in mineral content and fracture volume along the flow pathway. The extent of mineral dissolution was inferred based on relative mineral reactivity and observed effluent trends. Measured Na
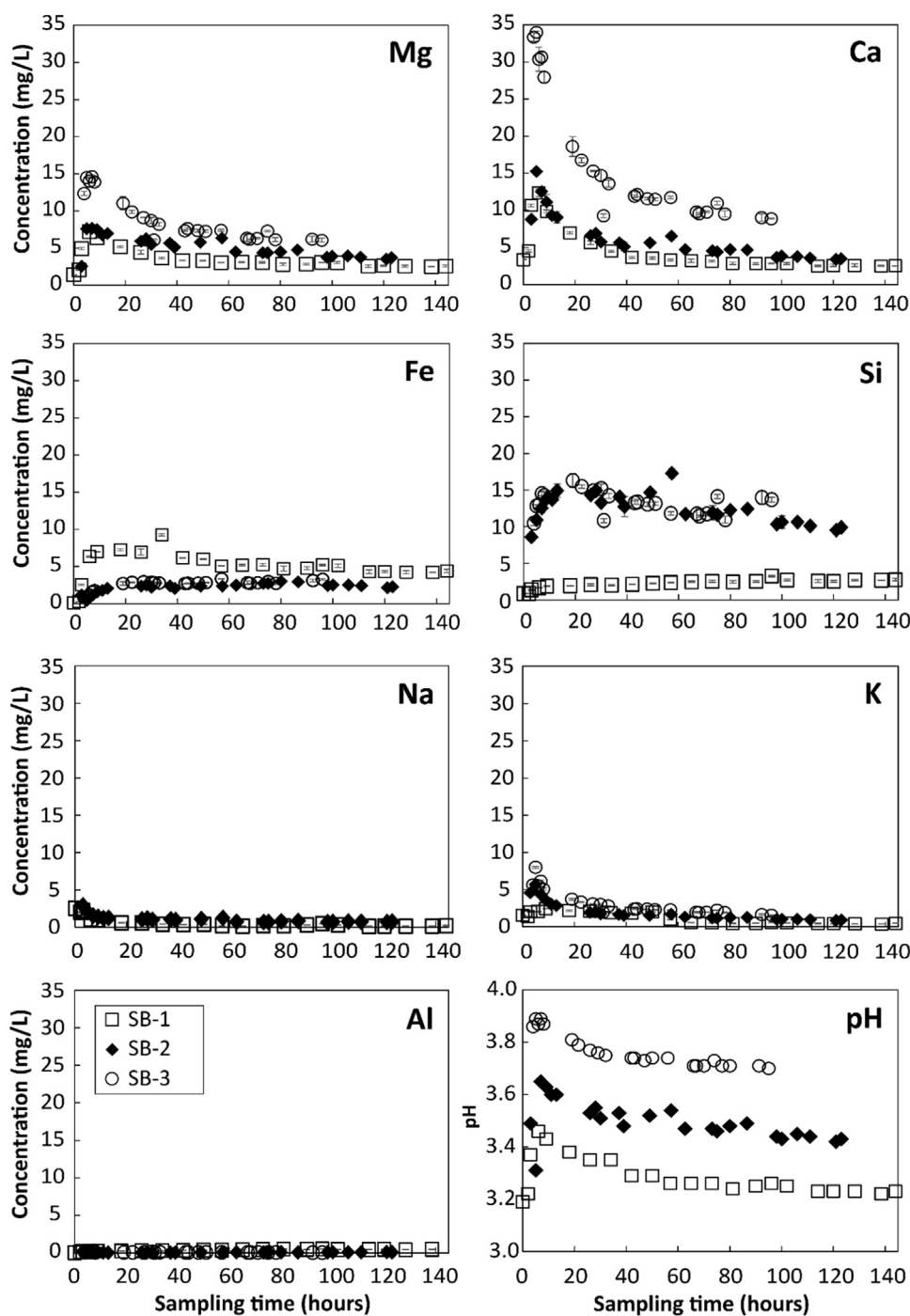


**Fig. 2.** EDS maps of (a) unserpentinized basalt (UB), and (b) serpentinized basalt (SB) plot Mg (red), Ca (green), and Al (blue). Pyroxene (px) is yellow, Olivine (olv) is red, plagioclase (feld) is light blue, and potassium-rich matrix (m) is dark blue. X-ray computed tomographic (XCT) images for UB and SB have been inserted to indicate the mineral distributions in both basalts. (For interpretation of the references to color in this figure legend, the reader is referred to the web version of this article.)

**Fig. 3.** Measured effluent chemistry and computed pH evolution for serpentinized basalt flow-through experiments conducted at 45° C (SB-1) or 100° C (SB-2, SB-3); 10 MPa $P_{CO2}$; and 20 MPa confining stress. Injected fluid was pure DI water (SB-1, SB-2) or DI with 13.8 mM NaCl and 1.2 mM $NaHCO_3$ (SB-3). Error bars for ICP-MS data correspond to relative standard deviations from three replicate measurements.

concentrations were significantly higher than could be accounted for with congruent plagioclase dissolution. The corresponding amount of Ca released assuming all Na dissolved stoichiometrically would result in little to no pyroxene dissolution based on the Ca balance. Because sodium was released preferentially from either plagioclase or from trace reactive glass phases, neither of which can be quantified here, it was excluded from the mass balance calculations. Al dissolves from the feldspars but given the lack of discernible K-feldspar grains, K was assumed to be released preferentially from the groundmass with only trace amounts of silicates and alumina, and all Al dissolution was attributed to plagioclase. The difference between the total measured moles of Ca in the effluent and the amount that would have dissolved stoichiometrically from this dissolved plagioclase volume is attributed to pyroxene, which was assumed to dissolve stoichiometrically per the

molar ratios established via WDS analyses of each basalt (Section 3.1). Finally, olivine dissolution was estimated based on a Mg balance with pyroxene, assuming any olivine that dissolved was primarily in the more reactive unserpentinized form. Mineral densities and molar weights based on WDS-derived stoichiometry were applied to convert moles to mineral volumes. Other trace minerals (e.g. chromite, ilmenite, apatite) were excluded from these calculations due to their low reactivity. The results of these calculations are provided in Table 2. For both samples, pyroxene contributed the most dissolved cations followed by olivine and plagioclase. Note that because dissolution in the experiments was incongruent, particularly at early stages, this approach may overestimate net dissolution of minerals that rapidly and preferentially release certain cations. Nonetheless, these calculations provide reasonable estimates of the relative reactivity of the major
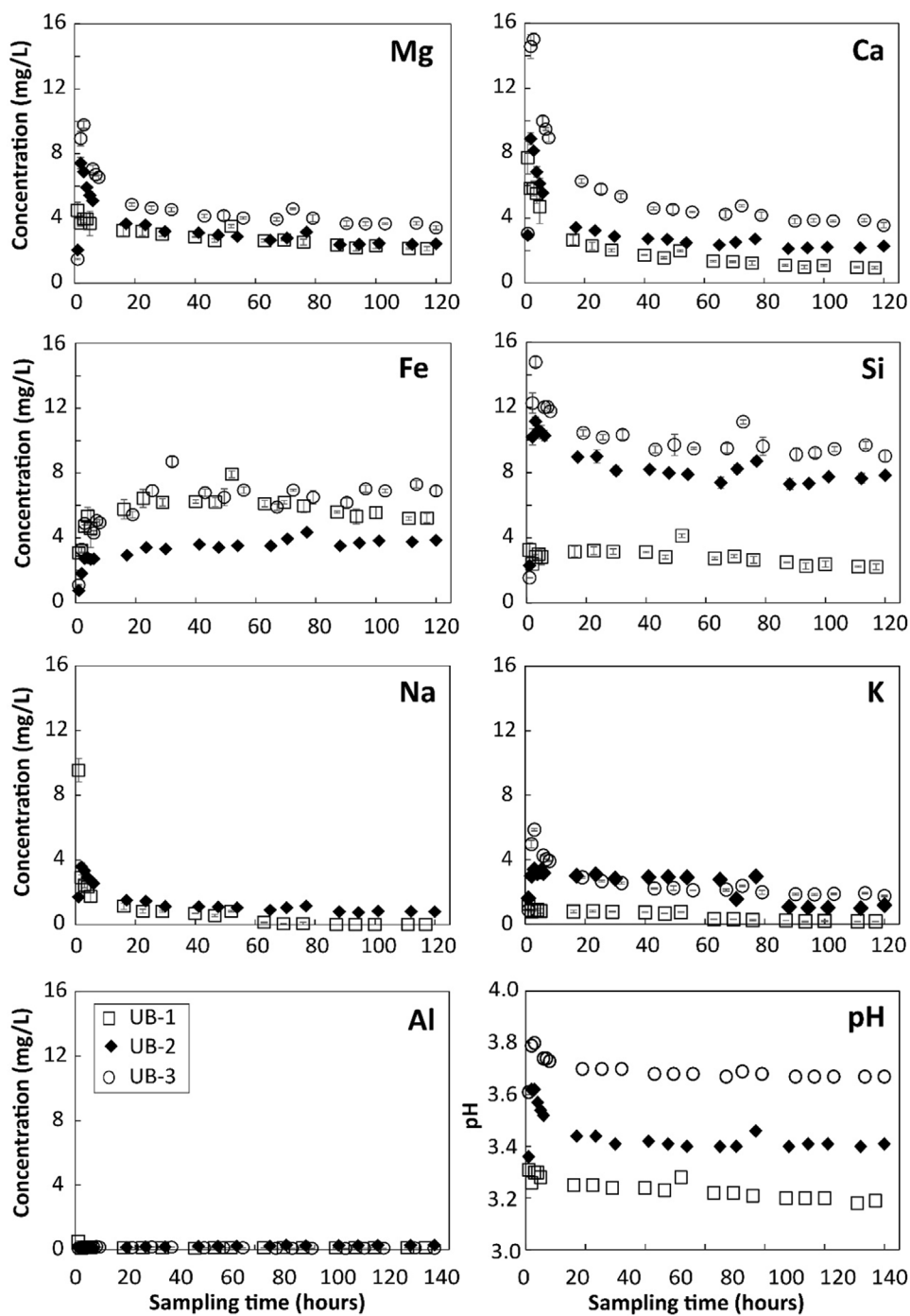
**Fig. 4.** Measured effluent chemistry and computed pH evolution for unserpentinized basalt flow-through experiments conducted at 45° C (UB-1) or 100° C (UB-2, UB-3); 10 MPa $P_{CO_2}$; and 20 MPa confining stress. Injected fluid was pure DI water (UB-1, UB-2) or DI with 13.8 mM NaCl and 1.2 mM NaHCO$_3$ (UB-3). Error bars for ICP-MS data correspond to relative standard deviations from three replicate measurements.
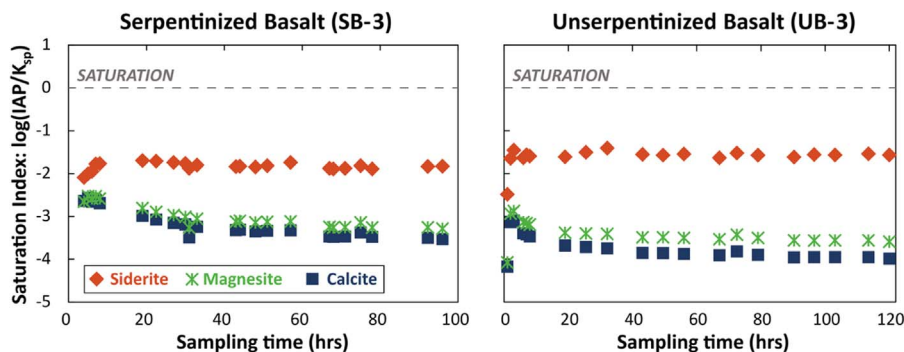


**Fig. 5.** Effluent saturation indices of major carbonate minerals based on measured divalent cation concentrations and calculated pH.

**Table 2**
Calculated mineral dissolution volumes based on mass balance calculations.

| Experiment | Pyroxene (mm³) | Olivine (mm³) | Plagioclase (mm³) | Total (mm³) |
|---|---|---|---|---|
| SB-1 | 5.03 | 1.16 | 1.00 | 7.19 |
| SB-2 | 6.66 | 1.37 | 0.14 | 8.17 |
| SB-3 | 12.9 | – | 0.10 | 13.0 |
| UB-1 | 2.48 | 1.43 | 0.26 | 4.17 |
| UB-2 | 2.33 | 1.85 | 0.51 | 4.68 |
| UB-3 | 7.58 | 0.43 | 0.25 | 8.26 |

minerals and net bulk volume changes driven by dissolution that are consistent with expected primary mineral abundance and reactivity in each sample.
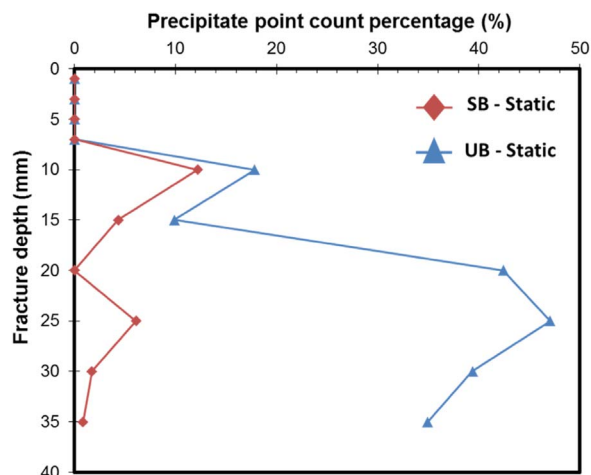
### 3.3. Static batch experiment

For both UB and SB, carbonate precipitates formed on the fracture surface after 6 weeks of reaction in $CO_2$-saturated water at 100 °C and 10 MPa. These precipitates, which were roughly 50 µm in size, were visible under the optical microscope (Fig. 6). The precipitates were distributed across the entire etched surface of the UB sample (Fig. 6(a–c)) while mm-scale clusters of precipitate were formed on localized areas on the SB surface (Fig. 6(d–f)).

Raman spectra of the precipitate showed diagnostic peaks at 281, 729 and 1084 cm$^{-1}$, which correspond to three vibrational modes of $CO_3^{2-}$ in siderite (Fig. 6(g)). SEM-EDS results indicate that the siderite contains minor amounts of Ca and Mg. A small amount of amorphous silica was also found on the surfaces of basalt and secondary carbonate precipitates. Point counting analysis (Fig. 7) showed that more siderite crystals were formed on the fracture surface for UB in comparison to SB. Carbonate point counts varied significantly with depth in each core and more carbonates were observed in the UB, potentially owing to the greater reactivity of unserpentinized olivine that was more abundant in the UB sample than in the SB sample. Siderite was not present along the fracture pathway in the 10 mm portion of the fracture closest to the $CO_2$-rich bulk solution. ICP-MS analysis of bulk solution showed that appreciable amounts of carbonate-forming cations including Mg, Ca, and Fe were present in the bulk solution post-reaction (Table 3).

## 4. Discussion

### 4.1. Impact of basalt composition and mineral spatial distribution on dissolution-precipitation reactions

Differences in bulk rock mineralogy as well as in reactive mineral



**Fig. 7.** Precipitate point count for unserpentinized basalt and serpentinized basalt cores reacted in 100 °C, 10 MPa $CO_2$-rich water for 6 weeks.

**Table 3**
Bulk solution chemistry after 6 weeks of reaction in static batch experiments.

| Core sample | Concentration (mM) | | | | | | |
|---|---|---|---|---|---|---|---|
| | Na | Mg | Al | Si | K | Ca | Fe |
| SB | 0.24 | 2.36 | 0.00 | 1.73 | 0.19 | 1.31 | 0.42 |
| UB | 0.63 | 1.88 | 0.01 | 2.34 | 0.28 | 1.13 | 1.32 |

locations and abundances between the two basalt samples contributed to the observed dissolution and precipitation behavior. In static experiments, carbonate spatial distribution trends (Fig. 7) were similar to those found in previous studies on carbonate mineral formation in a forsterite powder packed bed (Giammar et al., 2014; Xiong and Giammar, 2014). Precipitates were more localized in the SB sample, characterized by coarser and larger grains, while they formed more uniformly in the fine-grained UB sample. Siderite formed larger clusters in the SB sample and was generally localized on larger grains, whereas smaller crystals (~ 50 µm diameter) dispersed across the surface formed in the UB. Differences in mineral distribution and grain size between the two basalts (Fig. 2) explain why oxidized Fe appeared as small spots on the UB surface and as larger areas in the SB. The bulk mineralogy and reactive mineral abundance influenced which mineral precipitated in each sample, but the confluence of carbon entering the fracture and Fe diffusing out created highly supersaturated regions that likely determined where precipitation occurred. Similar differences in dissolution patterns between the two samples were observed in the flow-
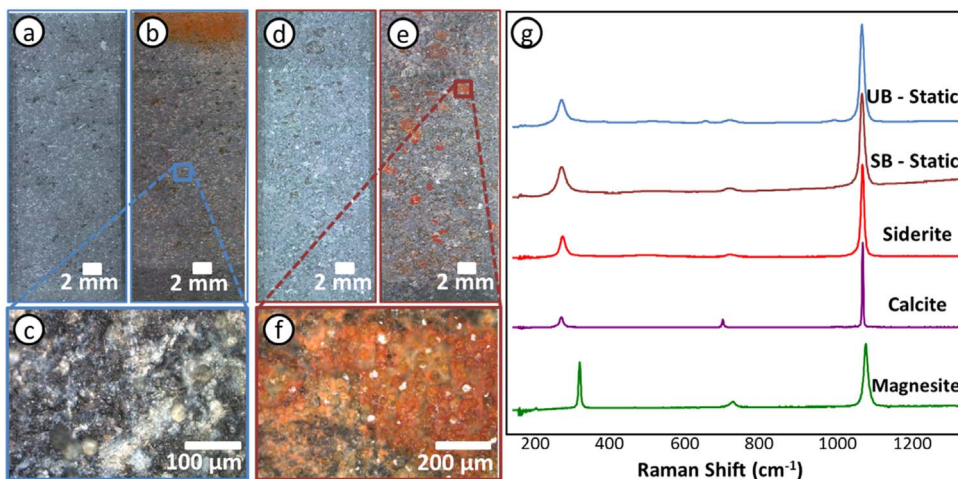


**Fig. 6.** Optical microscopic images of unserpentinized basalt (a) before reaction (b) after reaction, and (c) zoom-in on individual precipitates after reaction under static batch conditions at the end of 6 weeks, and serpentinized basalt (d) before reaction (e) after reaction (f) zoom-in on a precipitate cluster after reaction. (g) Raman spectra of carbonate precipitate formed in UB and SB. Spectra includes standards for siderite, calcite, and magnesite.
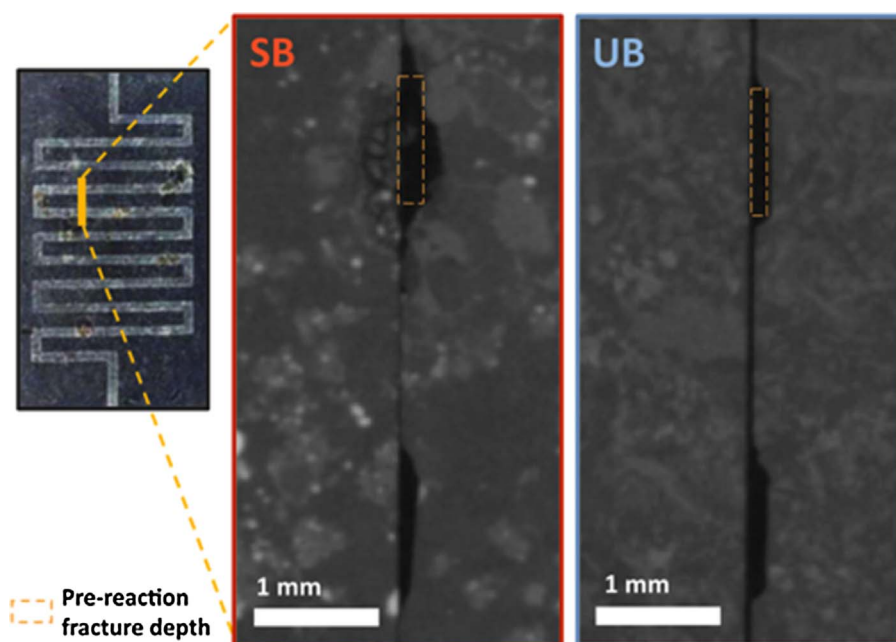
**Fig. 8.** Comparison of fracture dissolution patterns in the serpentinized (left) and unserpentinized (right) basalts for experiments conducted at 100 °C with added NaCl and NaHCO$_3$. Sections taken from XCT data perpendicular to the direction of flow contrast the uniform dissolution of the UB samples with non-uniform aperture growth observed in the SB.

through experiments. Fig. 8 compares post-reaction CT scans of both samples reacted in the experiments at 100 °C with added salinity and alkalinity. These cross sections (viewed perpendicular to fractures in the direction of flow) highlight the effect of initial mineral distribution in promoting non-uniform fracture dissolution. The fine grain size of the UB samples led to more uniform dissolution occurring along the fracture pathway, while the coarse grain size in the SB led to localized dissolution along larger reactive mineral grains. This localized dissolution pattern is similar to findings of previous studies in fractured carbonates in which preferential dissolution of minerals was attributed to differences in reaction kinetics (Ellis et al., 2011; Gouze et al., 2003). The results for both flow conditions investigated here indicate that variations in reactive mineral distribution and abundance may promote localized mineral precipitation.

Analogous to observations in the static experiments, mineral distribution and grain size variability created localized dissolution along flow paths but bulk mineralogy controlled the effluent chemistry. The abundance of pyroxene was similar in both basalt samples and effluent data suggests that it was the most reactive mineral phase. Greater Ca fractions in the diopside of the SB along with differences in the spatial distribution of pyroxene grains along the etched channel may have been the cause of effluent Ca concentrations approximately twice those of the UB. The consistency of higher effluent Ca concentrations in all SB experiments relative to UB suggests that bulk mineralogical differences were more significant than variations in mineral heterogeneity among cores of the same basalt. Although the UB samples had a greater amount of olivine, which has the fastest dissolution rate of the minerals present (Palandri and Kharaka, 2004), effluent Mg and Fe concentrations were generally highest in the SB experiments. Furthermore, pyroxene contributed more dissolution than olivine in both rocks on a mass basis (Table 2) due to its greater abundance. Dissolution of trace glass components in both rocks may have contributed greater amounts of dissolved minor cations than would be predicted by the bulk mineral phases, as differences in the structure of glass compared to crystals has been linked to more rapid release of cations from the bulk silica framework (Gislason and Eugster, 1987; Hamilton et al., 2000). In combination, the flow-through and static experiments confirmed that mineral dissolution and precipitation reactions were controlled by both the abundance and location of reactive mineral phases.

### 4.2. Roles of temperature and salinity in enhancing mineral reactivity

Elevated temperatures above typical *in-situ* CO$_2$ storage conditions and NaCl concentrations characteristic of basaltic aquifers enhanced dissolution for both basalt samples. Increased dissolution with increasing temperature has been well-demonstrated for individual minerals common in basalt, including olivine (Wang and Giammar, 2013), serpentines (Teir et al., 2007), and pyroxenes (Knauss et al., 1993). Schaef and McGrail (2009) found that kinetic dissolution rates of Columbia River flood basalts increased over 100 times from 25 to 90 °C under acidic to neutral pH conditions. Temperature and pH may also interact through positive feedback mechanisms, as Chen and Brantley (1998) demonstrated that the pH dependence of diopside dissolution is stronger at higher temperatures. This is consistent with the dissolution-enhancing effect of temperature observed here in low pH ranges (3.2–3.8), considering that dissolution rates of the reactive primary minerals increase with decreasing pH (Palandri and Kharaka, 2004).

The effect of temperature was most pronounced for dissolved silica, where concentrations were roughly four to five times higher at 100 °C than at 45 °C (Figs. 3 and 4). Molar ratios of the total dissolved cations to total dissolved silica were approximately one at the end of all experiments run at 100 °C and greater than one at 45 °C, indicating dissolution was sub-stoichiometric with respect to Si at lower temperatures. This is consistent with prior work on individual basaltic mineral dissolution rates that reported preferential release of cations from the bulk silica framework as seen for plagioclase (Casey and Westrich, 1991) and pyroxene (Zhang et al., 2013). Because divalent cation concentrations increased to a lesser extent than silica with increasing temperature, higher ratios of silica to cations were observed at 100 °C, indicating that while dissolution remained incongruent, release rates became more stoichiometric. Zhang et al. (2013) observed similar temperature-induced changes in a series of experiments measuring pyroxene dissolution rates, noting that Mg, Ca, Fe, and Al were released faster than Si from 25 to 100 °C, but Si dissolved most rapidly at higher temperatures. An earlier study observed analogous trends in albite dissolution whereby Na and Al were released faster than Si from 25 to 300 °C but dissolution became increasingly congruent with increasing temperature (Zhang, 2000). This was attributed to changes in water properties (i.e., a reduction in density and dielectric constant) and destruction of hydrogen bonds with increasing temperature that facilitate

breaking of covalently-bonded compounds (e.g., $SiO_2$) and hinder dissolution of ionic bonds (e.g., Ca−O, Mg−O) (Zhang et al., 2013). Incongruent dissolution becomes more pronounced at lower pH levels (Brantley et al., 2008), which was reflected here in the greater cation:silica ratios observed under lower pH conditions in the experiments run at 45 °C. While the effect of temperature was less dramatic, the increasing congruency of dissolution with increasing temperature was consistent for both serpentinized and unserpentinized basalts.

Although the effects of salinity and alkalinity were not isolated in the third set of experiments, the enhanced dissolution was likely promoted by NaCl. While Prigiobbe et al. (2009) concluded that changes in olivine dissolution rates under varying salt concentrations could be exclusively accounted for by changes in pH, the fact that greater dissolution was observed here in solutions with increased salinity and higher pH levels that would inhibit dissolution indicate NaCl may have a unique impact on dissolution rates under advective transport conditions. Wang and Giammar (2013) also found that NaCl enhanced the dissolution of forsterite, potentially by limiting the formation of passivating Si-rich layers. This effect could be significant even for the slight increase in salinity evaluated here, as prior work has demonstrated that amorphous silica dissolution rates increase by a factor of 21 in 0.05 M NaCl compared to DI water (Icenhower and Dove, 2000). While effluent samples were never supersaturated with respect to amorphous silica, Si-rich layers may have limited cation release in the first two experiments relative to the third. Prior work has shown that enhanced dissolution with salinity becomes more pronounced at higher salt concentrations (Wang and Giammar, 2013). However, in contrast to saline aquifers conventionally considered for $CO_2$ storage, salinity is unlikely to vary significantly across basalt aquifers at typical storage depths and thus may not be a major consideration for site selection (Reidel et al., 2002). This study confirms that temperature and salinity influence mineral dissolution and carbonation resulting from $CO_2$ injection in basalt reservoirs, but further work is needed to establish the sensitivity of dissolution rates to salt concentration and decouple the effect of the aqueous species contributing to salinity (e.g. NaCl vs KCl) from ionic strength.

### 4.3. Implications of fluid transport regimes for reaction location and extent

Under static batch conditions, rapid carbonation of the basalt cores occurred as Fe(II) was released from olivine ($Mg_{1.21}Fe_{0.78}Ca_{0.01}SiO_4$) in the unserpentinized basalt, forming siderite. Given that siderite also formed in the serpentinized basalt, which only contained 1% olivine, Fe-containing minerals such as pyroxene ($Ca_{0.83}Fe_{0.25}Mg_{0.85}Ti_{0.03}Al_{0.07}Si_{1.96}O_6$) and serpentine may serve as the dominant source for Fe(II). At 100 °C and 10 MPa, the solubility products (calculated in SUPCRT92) are −11.5, −9.41, and −9.22 for siderite, magnesite, and calcite, respectively. Because siderite has the lowest solubility, it precipitates more readily than magnesite or calcite given comparable concentrations of Fe, Mg, and Ca. Calcite, magnesite, and siderite saturation indices calculated from effluent chemistry data were less than zero throughout all flow-through experiments (Fig. 5). Siderite was closest to saturation, consistent with preferential siderite precipitation observed in the batch experiments. Under the same experimental conditions (100 °C with no added salt or alkalinity), static conditions induced secondary carbonate precipitation, while advection-dominated flow resulted in net dissolution.

The diffusive mass transport regime in the batch experiments likely created a chemical gradient in the dead-end fracture that influenced the distribution of carbonation products. Dissolved $CO_2$ diffused into the fracture while leached cations diffused out toward the bulk solution driven by concentration gradients, altering pH along the fracture. Zones closest to the bulk solution are anticipated to have a lower pH due to the proximity to the $CO_2$-acidified bulk solution, which can inhibit the fluid within the fracture from reaching saturation with respect to carbonate minerals. Deeper into the fracture, the accumulation of cations promotes a higher pH environment allowing carbonate minerals to

form once a critical super-saturation threshold is achieved. Carbonate mineral precipitation was maximal at depths of 10–25 mm from the open end of the core, which likely limited the extent of carbonate precipitation near the closed end of the fracture by restricting the supply of dissolved $CO_2$ (Fig. 7). These results are consistent with a 1-D reactive transport model developed by Giammar et al. (2014) for a static packed forsterite bed that predicted a peak location of supersaturation.

The net dissolution in the flow-through experiments indicates carbonation was limited due to the removal of divalent cation reaction products. Given that Ca, Mg, and Fe concentrations measured in the bulk solution from static experiments at 100 °C were lower than those measured in the corresponding flow-through experiments, the precipitation observed under static conditions resulted from mass transport limitations that allowed for greater pH buffering of the fluid within the fracture. This is consistent with prior work where precipitation was favored in diffusion-limited zones (Giammar et al., 2014). The presence of visible rust-colored iron oxides along the surface of the reacted cores could explain the absence of a sharp peak in Fe concentrations in the effluent data, as rapid oxidation of iron at the surface may have reduced the initial Fe release rates. Such Fe oxidation accompanying mineral carbonation has been reported under geological sequestration conditions (Luquot et al., 2012).

No measurable pressure differential was observed in any of the flow-through experiments, suggesting little change in permeability. Effluent solution analysis, mass balance, and fracture segmentation results all indicate net dissolution in the system, while saturation indices indicate precipitation was limited by the low pH resulting from continued $CO_2$ injection. For instance, if the pH had been approximately one unit higher in the UB-3 experiment (100 °C with added NaCl and $NaHCO_3$), effluent samples would have been supersaturated with respect to siderite throughout the experiment. Slower flow rates of $CO_2$-acidified fluids through fractured basalts might allow for sufficient pH buffering to promote secondary carbonate precipitation.

### 5. Conclusions

This study investigated how factors such as the mass transport regime and mineral distribution may influence the extent and location of dissolution and precipitation along fractures in basalt formations during $CO_2$ sequestration. Static batch experiments characterized by diffusive mass transport promoted siderite precipitation in both serpentinized and unserpentinized basalts in $CO_2$-acidified solutions, while flow-through studies using similar rocks resulted in net dissolution of silicate minerals with no indication of secondary mineral precipitation. Mineral dissolution was also enhanced in regions with a high abundance of reactive minerals, and the evolution of fracture geometry was influenced by mineral grain sizes along the fracture pathway. This pattern was mirrored under batch conditions where mm-scale clusters of siderite were found in the serpentinized basalt cores, while discrete crystals were distributed along the fracture in the unserpentinized basalt. While the bulk mineralogy of a basalt reservoir will influence the availability of divalent cations, diffusive mass transport conditions may be required to achieve mineral sequestration of injected $CO_2$. Hence, it is unlikely that significant mineralization will occur near wellbores or along interconnected fracture pathways due to strong advective flow of $CO_2$-acidified solutions. $CO_2$ mineral carbonation is most likely to occur in dead-end fractures, at distances further away from the wellbore where advective forces may be less dominant, or long after injection has ceased.

### Acknowledgements

Earth & Environmental Sciences and College of Literature, Science, and the Arts.

# References

Andreani, M., Luquot, L., Gouze, P., Godard, M., Hoisé, E., Gibert, B., 2009. Experimental study of carbon sequestration reactions controlled by the percolation of $CO_2$ – rich brine through peridotites. Environ. Sci. Technol. 43, 1226–1231. http://dx.doi.org/10.1021/es8018429.

Bachu, S., Adams, J.J., 2003. Sequestration of CO2 in geological media in response to climate change: capacity of deep saline aquifers to sequester CO2 in solution. Energy Convers. Manag. 44, 3151–3175. http://dx.doi.org/10.1016/S0196-8904(03)00101-8.

Bachu, S., 2000. Sequestration of CO2 in geological media: criteria and approach for site selection in response to climate change. Energy Convers. Manag. 41, 953–970. http://dx.doi.org/10.1016/S0196-8904(99)00149-1.

Benson, S.M., Cole, D.R., 2008. CO2 sequestration in deep sedimentary formations. Elements 4, 325–331. http://dx.doi.org/10.2113/gselements.4.5.325.

Berndt, M.E., Allen, D.E., Seyfried, W.E., 1996. Reduction of CO2 during serpentinization of olivine at 300 °C and 500 bar. Geology 24, 351–354. http://dx.doi.org/10.1130/0091-7613(1996)024<0351:ROCDSO>2.3.CO;2.

Brady, P., Carrol, S., 1994. Direct effects of CO2 and temperature on silicate weathering _possible implications for climate control. Geochem. Cosmochim. Acta 58 1953–1856.

Casey, W.H., Westrich, H.R., 1991. Dissolution rates of plagioclase at pH: 2 and 3. Am. Miner. 76, 211–217.

Chen, Y., Brantley, S.L., 1998. Diopside and anthophyllite dissolution at 25° and 90 °C and acid pH. Chem. Geol. 147, 233–248. http://dx.doi.org/10.1016/S0009-2541(98)00016-3.

Duan, Z., Sun, R., 2003. An improved model calculating CO2 solubility in pure water and aqueous NaCl solutions from 273 to 533 K and from 0 to 2000 bar. Chem. Geol. 193, 257–271.

Ellis, B., Peters, C., Fitts, J., Bromhal, G., McIntyre, D., Warzinski, R., Rosenbaum, E., 2011. Deterioration of a fractured carbonate caprock exposed to CO2-acidified brine flow. Greenh. Gases Sci. Technol. 1, 248–260. http://dx.doi.org/10.1002/ghg.25.

Frost, B.R., Beard, J.S., 2007. On silica activity and serpentinization. J. Petrol. 48, 1351–1368. http://dx.doi.org/10.1093/petrology/egm021.

Galwey, A.K., Brown, M.E., 2002. Application of the Arrhenius equation to solid state kinetics: can this be justified? Thermochim. Acta 386, 91–98. http://dx.doi.org/10.1016/S0040-6031(01)00769-9.

Giammar, D.E., Bruant, R.G., Peters, C.A., 2005. Forsterite dissolution and magnesite precipitation at conditions relevant for deep saline aquifer storage and sequestration of carbon dioxide. Chem. Geol. 217, 257–276. http://dx.doi.org/10.1016/j.chemgeo.2004.12.013.

Giammar, D.E., Wang, F., Guo, B., Surface, J.A., Peters, C.A., Conradi, M.S., Hayes, S.E., 2014. Impacts of diffusive transport on carbonate mineral formation from magnesium silicate-CO2 – water reactions. Environ. Sci. Technol. 48, 14344–14351. http://dx.doi.org/10.1021/es504047t.

Gislason, S.R., Eugster, H.P., 1987. Meteoric water-basalt interactions II: a field study in N.E. Iceland. Geochim. Cosmochim. Acta 51, 2841–2855. http://dx.doi.org/10.1016/0016-7037(87)90162-1.

Gouze, P., Noiriel, C., Bruderer, C., Loggia, D., Leprovost, R., 2003. X-ray tomography characterization of fracture surfaces during dissolution. Geophys. Res. Lett. 30, 1267. http://dx.doi.org/10.1029/2002GL016755.

Gysi, A.P., Stefánsson, A., 2012. Experiments and geochemical modeling of CO2 sequestration during hydrothermal basalt alteration. Chem. Geol. 306–307, 10–28. http://dx.doi.org/10.1016/j.chemgeo.2012.02.016.

Hänchen, M., Prigiobbe, V., Storti, G., Seward, T.M., Mazzotti, M., 2006. Dissolution kinetics of fosteritic olivine at 90–150 °C including effects of the presence of CO2. Geochim. Cosmochim. Acta 70, 4403–4416. http://dx.doi.org/10.1016/j.gca.2006.06.1560.

Hövelmann, J., Austrheim, H., Jamtveit, B., 2012. Microstructure and porosity evolution during experimental carbonation of a natural peridotite. Chem. Geol. 334, 254–265. http://dx.doi.org/10.1016/j.chemgeo.2012.10.025.

Hamilton, J.P., Pantano, C.G., Brantley, S.L., 2000. Dissolution of albite glass and crystal. Geochim. Cosmochim. Acta 64, 2603–2615.

Icenhower, J.P., Dove, P.M., 2000. The dissolution kinetics of amorphous silica into sodium chloride solutions: effects of temperature and ionic strength. Geochim. Cosmochim. Acta 64, 4193–4203. http://dx.doi.org/10.1016/S0016-7037(00)00487-7.

Intergovernmental Panel on Climate Change, 2005. IPCC Special Report on Carbon Dioxide Capture and Storage. Cambridge University Press, for the Intergovernmental Panel on Climate Change, Cambridge.

Jenkins, C.R., Cook, P.J., Ennis-King, J., Undershultz, J., Boreham, C., Dance, T., de Caritat, P., Etheridge, D.M., Freifeld, B., Hortle, A., et al., 2012. Safe storage of CO2 in a depleted gas field-the CO2CRC Otway Project. Proc. Natl. Acad. Sci. 109 (2), E35–E41.

Johnson, J.W., Oelkers, E.H., Helgeson, H.C., 1992. SUPCRT92: a software package for calculating the standard molal thermodynamic properties of minerals, gases, aqueous species, and reactions from 1 to 5000 bar and 0 to 1000 °C. Comput. Geosci. 18, 899–947.

Johnson, J.W., Nitao, J.J., Knauss, K.G., 2004. Reactive transport modelling of CO2 storage in saline aquifers to elucidate fundamental processes, trapping mechanisms, and sequestration partitioning. Geol. Storage Carbon Dioxide 233, 107–128. http://

Kelemen, P.B., Matter, J., Streit, E.E., Rudge, J.F., Curry, W.B., Blusztajn, J., 2011. Rates and mechanisms of mineral carbonation in peridotite: natural processes and recipes for enhanced, in situ CO2 capture and storage. Annu. Rev. Earth Planet. Sci. 39, 545–576. http://dx.doi.org/10.1146/annurev-earth-092010-152509.

Kelemen, P.B., Savage, H., Hirth, G., 2013. Reaction-driven cracking during mineral hydration, carbonation and oxidation. In: Poromechanics V: Proceedings of the Fifth Biot Conference on Poromechanics. ASCE. pp. 823–826.

Knauss, K.G., Nguyen, S.N., Weed, H.C., 1992. Diopside dissolution kinetics as a function of pH, CO2, temperature, and time. Geochem. Cosmochim. Acta 57, 285–294.

Knauss, K.G., Nguyen, S.N., Weed, H.C., 1993. Diopside dissolution kinetics as a function of pH, CO2, temperature, and time. Geochim. Cosmochim. Acta 57, 285–294. http://dx.doi.org/10.1016/0016-7037(93)90431-U.

Laidler, K.J., 1984. The development of the Arrhenius equation. J. Chem. Educ. 61, 494. http://dx.doi.org/10.1021/ed061p494.

Luquot, L., Andreani, M., Gouze, P., Camps, P., 2012. CO2 percolation experiment through chlorite/zeolite-rich sandstone (Pretty hill Formation–Otway Basin–Australia). Chem. Geol. 294–295, 75–88. http://dx.doi.org/10.1016/j.chemgeo.2011.11.018.

Matter, J.M., Takahashi, T., Goldberg, D., 2007. Experimental evaluation of in situ CO2-water-rock reactions during CO2 injection in basaltic rocks: implications for geological CO2 sequestration. Geochem. Geophys. Geosyst. 8, Q02001. http://dx.doi.org/10.1029/2006GC001427.

Matter, J.M., Stute, M., Snæbjörnsdottir, S.Ó., Oelkers, E.H., Gislason, S.R., Aradottir, E.S., Sigfusson, B., Gunnarsson, I., Sigurdardottir, H., Gunnlaugsson, E., Axelsson, G., Alfredsson, H.A., Wolff-Boenisch, D., Mesfin, K., Taya, D.F., de la, R., Hall, J., Dideriksen, K., Broecker, W.S., 2016. Rapid carbon mineralization for permanent disposal of anthropogenic carbon dioxide emissions. Science 352, 1312–1314. http://dx.doi.org/10.1126/science.aad8132.

McGrail, B.P., Schaef, H.T., Ho, A.M., Chien, Y.-J., Dooley, J.J., Davidson, C.L., 2006. Potential for carbon dioxide sequestration in flood basalts. J. Geophys. Res. Solid Earth 111, B12201. http://dx.doi.org/10.1029/2005JB004169.

McGrail, B.P., Schaef, H.T., Spane, F.A., Cliff, J.B., Qafoku, O., Horner, J.A., Thompson, C.J., Owen, A.T., Sullivan, C.E., 2017. Field validation of supercritical CO2 reactivity with basalts. Environ. Sci. Technol. Lett. 4, 6–10. http://dx.doi.org/10.1021/acs.estlett.6b00387.

Michael, K., Golab, A., Shulakova, V., Ennis-King, J., Allinson, G., Sharma, S., Aiken, T., 2010. Geological storage of CO2 in saline aquifers—a review of the experience from existing storage operations. Int. J. Greenh. Gas Control 4, 659–667. http://dx.doi.org/10.1016/j.ijggc.2009.12.011.

Nordbotten, J.M., Celia, M.A., Bachu, S., 2005. Injection and storage of CO2 in deep saline aquifers: analytical solution for CO2 plume evolution during injection. Transp. Porous Media 58, 339–360. http://dx.doi.org/10.1007/s11242-004-0670-9.

Palandri, J.L., Kharaka, Y.K., 2004. A Compilation of Rate Parameters of Water-mineral Interaction Kinetics for Application to Geochemical Modeling. DTIC Document.

Peuble, S., Godard, M., Luquot, L., Andreani, M., Martinez, I., Gouze, P., 2015. CO2 geological storage in olivine rich basaltic aquifers: new insights from reactive-percolation experiments. Appl. Geochem. 52, 174–190. http://dx.doi.org/10.1016/j.apgeochem.2014.11.024.

Prigiobbe, V., Costa, G., Baciocchi, R., Hänchen, M., Mazzotti, M., 2009. The effect of CO2 and salinity on olivine dissolution kinetics at 120 °C. Chem. Eng. Sci. 64, 3510–3515. http://dx.doi.org/10.1016/j.ces.2009.04.035.

Reidel, S.P., Spane, F.A., Johnson, V.G., 2002. Natural Gas Storage in Basalt Aquifers of the Columbia Basin, Pacific Northwest USA: A Guide to Site Characterization. Pacific Northwest National Laboratory (PNNL), Richland, WA (US).

Rosenbauer, R.J., Thomas, B., Bischoff, J.L., Palandri, J., 2012. Carbon sequestration via reaction with basaltic rocks: geochemical modeling and experimental results. Geochim. Cosmochim. Acta 89, 116–133. http://dx.doi.org/10.1016/j.gca.2012.04.042.

Schaef, H.T., McGrail, B.P., 2009. Dissolution of Columbia River Basalt under mildly acidic conditions as a function of temperature: experimental results relevant to the geological sequestration of carbon dioxide. Appl. Geochem. 24, 980–987. http://dx.doi.org/10.1016/j.apgeochem.2009.02.025.

Schaef, H.T., McGrail, B.P., Owen, A.T., 2010. Carbonate mineralization of volcanic province basalts. Int. J. Greenh. Gas Control 4, 249–261. http://dx.doi.org/10.1016/j.ijggc.2009.10.009.

Shaw, J., Bachu, S., 2002. Screening, evaluation, and ranking of oil reservoirs suitable for CO2-flood EOR and carbon dioxide sequestration. J. Can. Pet. Technol. 41.

Sissmann, O., Brunet, F., Martinez, I., Guyot, F., Verlaguet, A., Pinquier, Y., Daval, D., 2014. Enhanced olivine carbonation within a basalt as compared to single-phase experiments: reevaluating the potential of $CO_2$ mineral sequestration. Environ. Sci. Technol. 48, 5512–5519. http://dx.doi.org/10.1021/es405508a.

Sokama-Neuyam, Y.A., Ursin, J.R., 2015. $CO_2$ well injectivity: effect of viscous forces on precipitated minerals. Presented at the International Petroleum Technology Conference International Petroleum Technology Conference. http://dx.doi.org/10.2523/IPTC-18268-MS.

Szulczewski, M.L., MacMinn, C.W., Herzog, H.J., Juanes, R., 2012. Lifetime of carbon capture and storage as a climate-change mitigation technology. Proc. Natl. Acad. Sci. 109, 5185–5189. http://dx.doi.org/10.1073/pnas.1115347109.

Teir, S., Revitzer, H., Eloneva, S., Fogelholm, C.-J., Zevenhoven, R., 2007. Dissolution of natural serpentinite in mineral and organic acids. Int. J. Miner. Process. 83, 36–46. http://dx.doi.org/10.1016/j.minpro.2007.04.001.

Van Pham, T.H., Aagaard, P., Hellevang, H., 2012. On the potential for CO2 mineral storage in continental flood basalts −PHREEQC batch- and 1D diffusion-reaction simulations. Geochem. Trans. 13, 5. http://dx.doi.org/10.1186/1467-4866-13-5.

Wang, F., Giammar, D.E., 2013. Forsterite dissolution in saline water at elevated

temperature and high $CO_2$ pressure. Environ. Sci. Technol. 47, 168–173. http://dx.doi.org/10.1021/es301231n.

Wells, R., Giammar, D., Skemer, P., 2016. Sample Library of Natural and Artificial Basalts. Basalt_Library_GCS_.

Whittaker, S., Rostron, B., Hawkes, C., Gardner, C., White, D., Johnson, J., Chalaturnyk, R., Seeburger, D., 2011. A decade of CO2 injection into depleting oil fields: monitoring and research activities of the IEA GHG Weyburn-Midale CO2 Monitoring and Storage Project. Energy Procedia 4, 6069–6076. http://dx.doi.org/10.1016/j.egypro.2011.02.612.

Wigand, M., Carey, J.W., Schütt, H., Spangenberg, E., Erzinger, J., 2008. Geochemical effects of CO2 sequestration in sandstones under simulated in situ conditions of deep saline aquifers. Appl. Geochem. 23, 2735–2745. http://dx.doi.org/10.1016/j.apgeochem.2008.06.006.

Xiong, W., Giammar, D., 2014. Forsterite carbonation in zones with transport limited by diffusion. Environ. Sci. Technol. Lett. 1, 333–338. http://dx.doi.org/10.1021/ez500182s.

Xu, T., Apps, J.A., Pruess, K., 2005. Mineral sequestration of carbon dioxide in a sandstone-shale system. Chem. Geol. 217, 295–318. http://dx.doi.org/10.1016/j.chemgeo.2004.12.015.

Yang, L., Steefel, C.I., Bechtel, H., 2013. Microfluidic and capillary tube experimental study of forsterite carbonation by CO2 bearing fluids. AGU Fall Meet. Abstr. 41.

Zhang, R., Zhang, X., Guy, B., Hu, S., De Ligny, D., Moutte, J., 2013. Experimental study of dissolution rates of hedenbergitic clinopyroxene at high temperatures: dissolution in water from 25 °C to 374 °C. Eur. J. Miner. 25, 353–372. http://dx.doi.org/10.1127/0935-1221/2013/0025-2268.

Zhang, X., 2000. Kinetics of hydrothermal reactions of minerals in near-critical and supercritical water. Acta Geol. Sin. – Engl. Ed. 74, 400–405. http://dx.doi.org/10.1111/j.1755-6724.2000.tb00483.x.

Zhu, W., Fusseis, F., Lisabeth, H., Xing, T., Xiao, X., De Andrade, V., Karato, S., 2016. Experimental evidence of reaction-induced fracturing during olivine carbonation. Geophys. Res. Lett. 43http://dx.doi.org/10.1002/2016GL070834. (2016GL070834).